PhotoniX

RESEARCH Open Access

Wavelength-multiplexed orbital angular momentum meta-holography

Jaehyuck Jang[1,2†], Seong-Won Moon[3†], Joohoon Kim[3†], Jungho Mun[3,4], Stefan A. Maier[5,6], Haoran Ren[5] and Junsuk Rho[1,3,7,8,9*]

†Jaehyuck Jang, Seong-Won Moon and Joohoon Kim these authors are equally contributed.

*Correspondence: jsrho@postech.ac.kr

[1] Department of Chemical Engineering, Pohang University of Science and Technology (POSTECH), Pohang 37673, Republic of Korea
[2] Department of Materials Science and Engineering, Stanford University, Stanford, CA 94305, USA
[3] Department of Mechanical Engineering, Pohang University of Science and Technology (POSTECH), Pohang 37673, Republic of Korea
[4] School of Electrical and Computer Engineering, Purdue University, West Lafayette, IN 47907, USA
[5] School of Physics and Astronomy, Monash University, Melbourne, VIC 3800, Australia
[6] Department of Physics, Imperial College London, London SW7 2AZ, UK
[7] Department of Electrical Engineering, Pohang University of Science and Technology (POSTECH), Pohang 37673, Republic of Korea
[8] POSCO-POSTECH-RIST Convergence Research Center for Flat Optics and Metaphotonics, Pohang 37673, Republic of Korea
[9] National Institute of Nanomaterials Technology (NINT), Pohang 37673, Republic of Korea

Abstract

The field of high-bandwidth holography has been extensively studied over the past decade. Orbital angular momentum (OAM) holography, which utilizes vortex beams with theoretically unbounded OAM modes as information carriers, showcases the large capacitance of hologram storage. However, OAM holography has been limited to a single wavelength, restricting its potential for full-color holography and displays. In this study, we propose wavelength and OAM multiplexed holography that utilizes the multiple dimensions of light—wavelength and OAM—to provide a multi-color platform that expands the information capacity of holographic storage devices. The proposed wavelength-OAM multiplexed holography is physically realized by a metasurface, the state-of-the-art optical element consisting of an array of artificially engineered nanostructures. Hydrogenated silicon meta-atoms, the constituents of the metasurface, are engineered to possess wavelength selectivity by tailoring the dispersion of polarization conversion. These meta-atoms are used to encode the calculated OAM-preserved phase maps based on our design. The sampling grid of the phase map is rotated by 45°, which effectively suppress higher-order diffraction, providing a great strategy for achieving large field-of-view (FOV) holography. We successfully demonstrate six holographic images that are selectively reconstructed under the illumination of light with specific wavelengths ($\lambda = 450$, 635 nm) and topological charges ($l = -2$, 0, 2), without high-order diffraction. Our work suggests that ultrathin meta-holograms can potentially realize ultrahigh-bandwidth full-color holography and holographic video displays with large FOV.

Keywords: Metasurface, Meta-holography, Wavelength-multiplexed holography, OAM holography

Introduction

The field of high-capacity holography has attracted significant attention, owing to the growing interest in optical devices for applications such as optical encryption [1–4], optical data storage [5–7], and augmented and virtual reality [8–11]. In response, researchers have explored a range of input beam properties, including wavelength, angle of incidence, polarization, and angular momentum (AM), to enhance the capacity for information storage. Among these properties, orbital angular momentum (OAM),

characterized by its helical wavefront, has emerged as a powerful tool for optical encoding, primarily due to its theoretically unbounded topological charge.

OAM holography leverages the OAM of light as an information carrier. By employing computer-generated holograms (CGH) through an iterative process, it becomes possible to design a phase profile that accommodates multiple holographic images [12–14]. Each of these images is visible exclusively under specific topological charges of the incident vortex beam. However, this approach does not inherently address the issue of perturbing the helical wavefront carried by the incident OAM beam in traditional digital holography. In simpler terms, the OAM property of the incoming beam is not preserved in the image plane, presenting a fundamental challenge to the realization of OAM holography. To overcome this limitation, the concept of OAM-conserved and multiplexed holograms has been introduced [15], which involves the incorporation of a sampling array. This innovation allows for the utilization of unbounded topological charges, thereby enhancing the number of holographic images encoded within the holographic device. Following these pioneering developments, researchers have sought to expand the multiplexing capabilities by introducing factors such as incoherent light [16], nonlinear effects [17], polarization [18], and spatial beams like Laguerre-Gaussian [19], Hermite-Gaussian [20], and helico-conical beams [21]. On the other hand, multiplexing OAM holograms within the wavelength domain has just begun to attract interest in the field [22].

A metasurface, which consists of a one- or two-dimensional array of nanostructures, serves as an excellent platform for the creation and encoding of phase profiles derived from CGH with a high spatial resolution [23–25]. Depending on the specific design, the individual structural units of the metasurface, referred to as meta-atoms, can exhibit unique optical characteristics [26–28], including resonant frequency, spectral selectivity, polarization sensitivity, chirality, and nonlinearity. By manipulating the resonances of all-dielectric nanostructures within the metasurface, it becomes possible to engineer optical elements that are both achromatic and dispersive [29, 30]. Consequently, we anticipate that metasurfaces can be effectively employed to realize wavelength-multiplexed OAM holography. This multiplexed manipulation was previously achieved using a multiplexed coherent pixel approach [22], which inevitably makes the pixel larger than the wavelength and generate unwanted high-order diffraction to free space. Moreover, having multiple metaatoms in a single pixel can lead to uneven intensity in the reconstructed image, thus requiring the development of methods to maintain hologram quality when reconstructed.

In this study, we present a wavelength-multiplexed OAM holographic device. This device is designed to encode multiple holographic images, each of which can be reconstructed when illuminated with light of a specific wavelength and a predetermined topological charge associated with a vortex beam. To ensure uniform intensity in the reconstructed images, we proposed a new encoding method using multi-step iterative algorithms. We selected target wavelengths within the wavelength domain, specifically 635 and 450 nm, corresponding to the primary colors in the visible spectrum. The designed metasurface consists of pixels with an effective period smaller than the minimum wavelengths to suppress the high-order diffraction. For our proof of concept, we have focused on vortex charges of -2, 0, and 2. It is important to note that these selections do not impose an inherent upper limit on the storage potential of our device. In

our demonstration, we have encoded six distinct images onto our holographic device, and we have successfully reconstructed these images under specific conditions of incident light, as depicted in Fig. 1.

Results

Design of wavelength-selective meta-atoms

To achieve both multiplexing in wavelength and OAM domains, the key lies in the development of specialized optical elements tailored to interact selectively with particular wavelengths. We have found a solution in the form of metasurfaces. The constituent meta-atoms possess the unique ability to shape wavefronts across various dimensions. In simple terms, these meta-atoms exhibit a strong interaction with light at specific wavelengths. We have selected hydrogenated amorphous silicon (Si) as the constituent material for our meta-atom. This choice stems from the fact that Si possesses a low extinction coefficient and a moderately refractive index within the visible spectrum (Fig. 2b) [31].

To simultaneously maintain low absorption and high efficiency, we have devised a vertical truncated wavelength structure as our meta-atom. This meta-atom assumes the form of a cuboid with specific dimensions: height (H), length (L), width (W), and a lattice constant (P), as illustrated in Fig. 2a. We have denoted the meta-atoms designed for wavelengths of 450 nm and 635 nm as MA1 ($L = 130$ nm; $W = 50$ nm) and MA2 ($L = 260$ nm; $W = 130$ nm), respectively. These meta-atoms exhibit wavelength selectivity, functioning as birefringent waveguides, as demonstrated in Fig. 2c. When light with x polarization is introduced into the waveguide, it undergoes a conversion to y-polarization upon outcoupling. Importantly, this polarization conversion within MA1 to MA2 exclusively occurs at the intended wavelength for each meta-atom (see Fig. 2c). This phenomenon is further underpinned by the calculation of conversion efficiency spectra (Fig. 2b), which highlights the dominant conversion efficiency of each meta-atom at its target wavelength. It is worth noting that the lower efficiency observed in MA1 is primarily attributed to the inherent absorption characteristics of silicon in blue regime (see Fig. 2b), which could be even more exacerbated in other silicon materials.

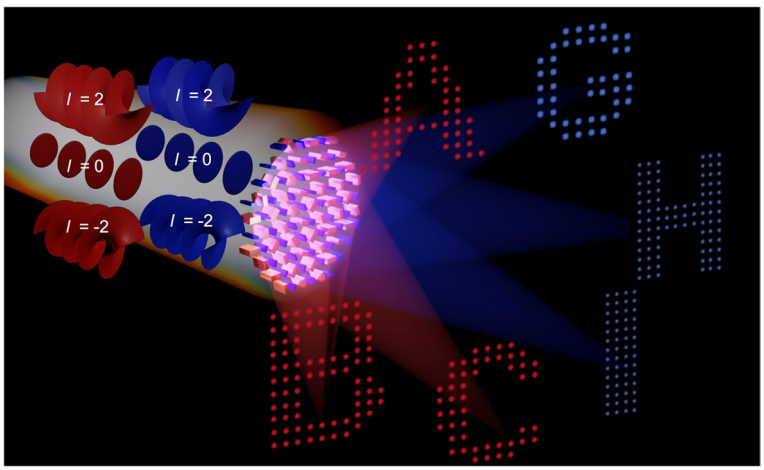

Fig. 1 Principle of wavelength-multiplexed OAM holography. The holograms encoded in the interleaved metasurface are reconstructed at specific wavelengths and topological charges of the vortex beam

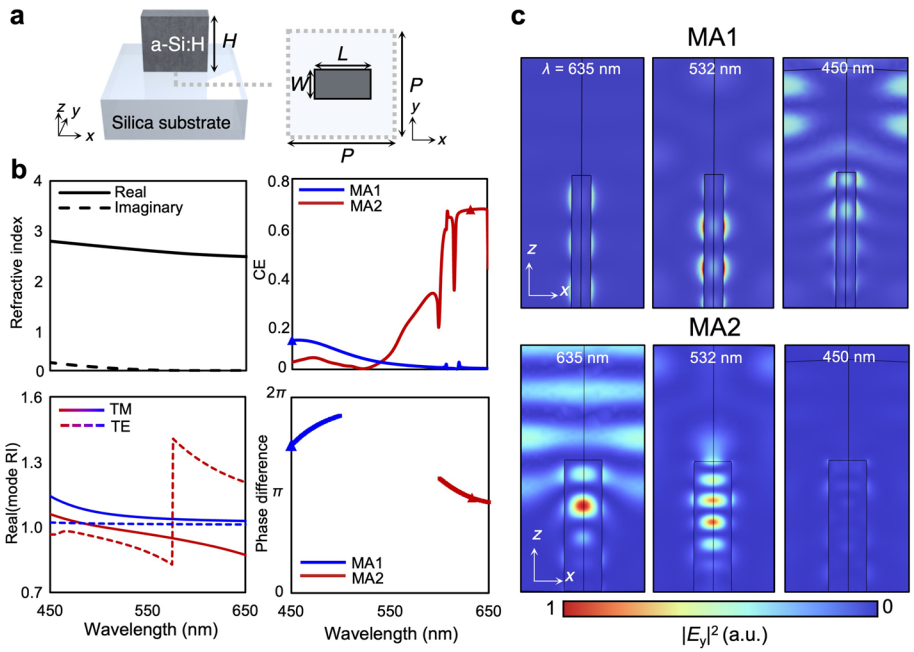

Fig. 2 Design principle of wavelength-selective Si meta-atom. **a** Schematics of the Si meta-atom. **b** Refractive indices of Si (Solid: real; Dashed: imaginary part) and spectra of conversion efficiency, mode refractive index (Solid: TM; Dashed: TE mode), and phase difference between TM and TE mode propagation of the meta-atoms. Blue: MA1; Red: MA2. Triangular mark represents the values at target wavelength. **c** Distribution of the *y*-component of electric field under illumination with *x*-polarized light at specific wavelengths

The dispersion in the polarization conversion efficiency spectrum stems from the phase mismatch that arises between the dominant transverse magnetic (TM) and transverse electric (TE) modes within the meta-atom [32]. To compute this phase mismatch, we initially determine the mode refractive indices of the dominant TM and TE modes within our meta-atom geometry, as depicted in Fig. 2b. Subsequently, the phase difference is calculated as follows:

$$\Delta\varphi = \varphi_{\mathrm{TM}} - \varphi_{\mathrm{TE}} = k_0 H\left(n_{eff}^{TM} - n_{eff}^{TE}\right), \tag{1}$$

where $\varphi_{\mathrm{TM}\ or\ TE}$ is phase delay of TM or TE mode, k_0 is wavenumder, and $n_{eff}^{TM\ or\ TE}$ is mode refractive index of TM or TE mode. As illustrated in the phase difference spectrum (Fig. 2b), the conversion efficiency is maximized at the wavelength where the phase difference approaches π. A phase difference of π indicates that the meta-atom possesses a remarkable ability to convert light, effectively serving as a localized half-wave plate. Conversely, at wavelengths outside the target range, this meta-atom exhibits limited capabilities as a localized half-wave plate due to the presence of phase mismatch. This phenomenon serves as the fundamental basis for the wavelength-selectivity of our meta-atom.

Design of an OAM-selective and OAM-multiplexed hologram

Figure 3 illustrates the process of creating the OAM-conserved hologram (OCH), the OAM-selective hologram (OSH), and OAM-multiplexed hologram (OMH). To design an OCH, the target image object should be precisely sampled using a 2D Dirac comb function (Fig. 3a). The desired image is obtained by multiplying the image object by a two-dimensional (2D) Dirac comb in the image plane [33]. This approach mitigates interference between adjacent pixels of the reconstructed holographic images. The sampling constant (p) of the 2D Dirac comb is determined based on the size of the doughnut-shaped intensity distribution in the spatial frequency domain of the spiral phase, as depicted in Fig. 3a and S1. In this study, these sampling parameters are chosen according to the largest radius of the kernel in the image plane. As a result, each pixel in the reconstructed image faithfully preserves the properties of the incident OAM beam. Given that the size of a pixel's intensity distribution is proportional to OAM modes l, the sampling constant is influenced by the wavelength of the incident light, the effective numerical aperture of the hologram, and the topological charge of the OAM modes (Fig. 3a and

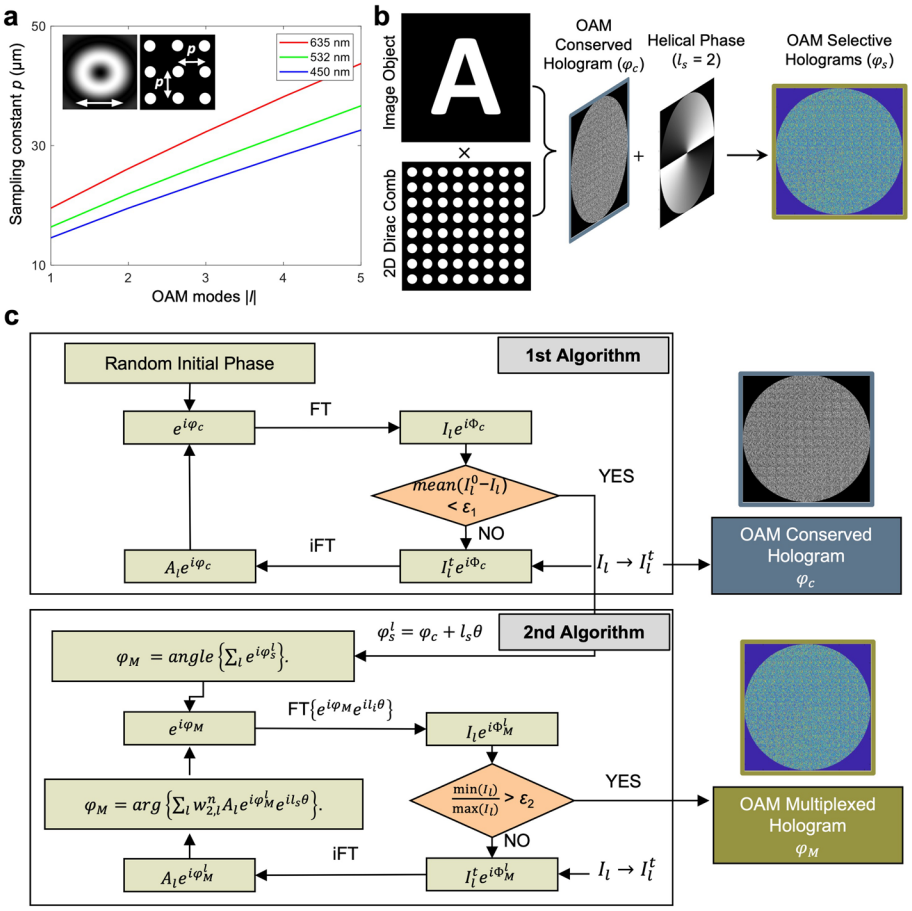

Fig. 3 Design principle of OAM holography. **a** Calculated sampling constant (p) for absolute value of the orbital angular momentum (OAM) mode $|l|$ at the 450, 532, and 635 nm, respectively. **b**–**d** Schematic of design methods: (**b**) OAM conserved and selective hologram, (**c**) Flowchart of a phase retrieval algorithm based on modified GS algorithms for OAM conserved hologram, OAM selective hologram, and OAM multiplexed hologram

S1). The effective numerical aperture of the hologram is set to 0.05 for wavelengths of 450 nm and 635 nm. To achieve a lensless Fourier holographic image, a Fourier transform lens phase is added to the hologram.

The design process of OCH, OSH, and OMH is depicted in Fig. 3b and c [15]. The OCH (φ_c) with random phase as initial value propagates forward by Fourier transform to obtain reconstructed field $I_l e^{i\Phi_c}$ in image domain, where l is corresponding to specific OAM modes of the OSH. After compared I_l to the original image (I_l^0), I_l is replaced to calculated intensity constraint (I_l^t). To guarantee a uniform intensity in each pixel of reconstructed images, a two-dimensional weighting factor is applied to I_l^t in each phase retrieval iteration. The weighting factor is expressed by

$$w_{1,l}^n = w_{1,l}^{n-1} \frac{\sum_{i=1}^{M} abs\left(E\left(x_i, y_i\right)\right)}{M\, abs\left(E\left(x_i, y_i\right)\right)} \; (w_{1,l}^0 = 1), \tag{2}$$

where M and E means total pixel number of sampled image and electric field distribution at the sampling position in the reconstructed image. n and $w_{1,l}^0$ represent the iteration number and initial value of weighting factor. I_l^t, which is expressed as Hadamard product of $w_{1,l}^n$ and the intensity of original image I_l^0, is updated and multiplied to $e^{i\Phi_c}$ in each phase retrieval iteration. By inverse Fourier transform and extracting phase component, phase only hologram φ_c is obtained by 1st modified GS algorithm that guarantee a unified intensity distribution of reconstructed holographic images. 1st modified GS algorithm finishes iteration when the mean of difference between original image and reconstructed image is less than ϵ_1 (0.01 in this work), and obtains φ_c.

Second, based on φ_c, OSH φ_s and OMH φ_M are obtained by 2nd modified GS algorithm (Bottom in Fig. 3c). To create an OSH, the phase profile of a spiral phase plate denoted as $l_s\theta$, where θ represents the azimuthal angle in the cylindrical coordinate is added on to OCH (Fig. 3b). Consequently, the total topological charge of light after passing through OSH can be expressed as $l_t = l_s + l$, where l_s denotes the topological charge of the spiral phase plate and l represents the topological charge of the incident OAM beam. When an OAM beam with an opposite topological charge ($l = -l_s$) is employed, the total topological charge becomes zero. Consequently, the electric field of each pixel is excited to the fundamental mode, resulting in a peak intensity in the reconstructed holographic image for a given OAM mode with the opposite topological charge. As a result, a significant intensity difference between the fundamental mode and high-order modes leads to OAM-selective holographic images. Then, the phase profile of OAM-multiplexed hologram is obtained as sum of OAM-selective holograms, which can reconstruct distinct holographic images for the desired OAM beams. In our study, we demonstrate both OAM selectivity and OAM multiplexity in a meta-hologram, particularly for specific cases of incident OAM beams with topological charges of $l = -2$, 0, and 2. OSHs corresponding to desired l can be expressed as $\varphi_s^l = \varphi_c + l_s\theta$. OSHs are obtained through each design process based on 1st GS algorithm, for example, 1st GS algorithm works three times to retrieve φ_s^{-2}, φ_s^0, and φ_s^2 corresponding to I_{-2}^0, I_0^0, and I_2^0, respectively. To obtain clearer OAM-multiplexed holographic images, here, we applied to 2nd modified GS algorithm (Bottom in Fig. 3c) for reducing fluctuation of uniform intensity in a holographic image and intensity difference among OAM-multiplexed holographic images. The initial value of

φ_M, $angle\left\{\sum_l e^{i\varphi_s^l}\right\}$, which is phase term of sum of OSHs obtained in 1st GS algorithm, is fed into the 2nd GS algorithms. Then, each holographic image ($I_l e^{i\Phi_M^l}$) is reconstructed through Fourier transform considering desired l of incident OAM beams. Hadamard product of the weighting factor $w_{1,l}^n$ in Eq. 2 is also applied to target image I_l^t, which guarantee intensity uniform of reconstructed images in the process of retrieving φ_M. Complex amplitudes ($A_l \varphi_m^l$), which is inverse Fourier transform of $I_l^t e^{i\Phi_M^l}$ are summation after multiplying second weighting factors ($w_{2,l}^n$). The second weighting factor is expressed by

$$w_{2,l}^n = w_{2,l}^{n-1} \frac{\sum_{k=1}^{3} abs\left(\bar{E}_k(x,y)\right)}{3\, abs\left(\bar{E}_k(x,y)\right)} \quad (w_{2,l}^0 = 1), \tag{3}$$

where k and n indicate number of three multiplexing holographic images and iteration number, respectively. $\bar{E}_k$ represents mean of normalized multiplexed holographic image corresponding to the number k. The second weighting factors guarantee same intensities between holographic images. The ratio of minimum and maximum intensity in all reconstructed OAM-multiplexed holographic images is set to ϵ_2 (0.99 in this work). As a result, a phase-only OAM multiplexed hologram with uniform intensity distribution can be obtained (Figure S2).

Wavelength-multiplexed OAM holography

To achieve multiplexed holographic images from a single meta-hologram, three OSHs with corresponding OAM modes are designed and combined into single phase

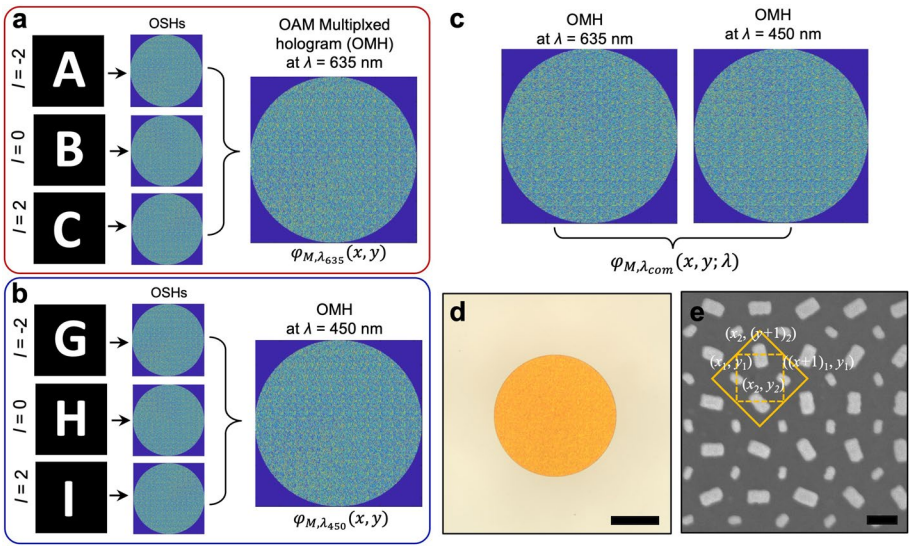

Fig. 4 OAM multiplexed hologram at (**a**) 635 nm and (**b**) 450 nm. (**c**) wavelength-multiplexed OAM holograms working at the wavelength of 450 and 635 nm. Fabricated metasurface for wavelength-multiplexed OAM holograms visualized by (**d**) optical microscope and (**e**) scanning-electron microscope. Scale bar: 100 μm and 250 nm, respectively

map. Figure 4a and b illustrate the design schematic of the OMH with topological charges of $l = -2,0$, and 2 at wavelengths of 635 nm and 450 nm, respectively. These two OMHs are then combined to multiplex them in wavelength domain as well (See Fig. 4c).

To spatially combine the two phase maps into the wavelength-OAM multiplexed phase map $\varphi_{M,\lambda_{com}}$, the (x, y) pixel of $\varphi_{M,\lambda_{com}}$ is super-pixelized into (x_1, y_1) and (x_2, y_2) subpixels. The phase value at subpixel (x_1, y_1) is filled by that of the OAM-multiplexed phase map at 450 nm $\varphi_{M,\lambda_{450}}(x, y)$, then the phase at subpixel (x_2, y_2) is filled by that of OAM-multiplexed phase map at 635 nm $\varphi_{M,\lambda_{635}}(x, y)$. The straightforward method to achieve this with meta-atoms is to introduce a unit pixel with a 2-by-2 grid consisting of two identical MA1s and MA2s. In this 2-by-2 grid, the solid outline box in Fig. 4e represents the unit pixel that consist of four meta-atoms (two of each are identical), and the periodicity of the unit pixel becomes 2^*P, which inevitably induces high-order diffraction to far field. This hamper the advantage of the metasurface with subwavelength pixel, which is to modulate 0th order of incident light without high-order diffraction, thereby potentially enabling 180°-field-of-view hologram [24]. To preserve this benefit, we rotate the sampling grid by 45° to create an effective period $\sqrt{2}P$ smaller than minimum wavelength used in this system (see the box with dashed outline in Fig. 4e). In this unit pixel, only one MA1 and MA2 exist. The wavelength-dependent OAM- multiplexed hologram sampled with the rotated grid is then physically realized by interleaving wavelength-selective MA1 and MA2 (Fig. 4d and e). The detailed analysis on the high-order diffraction of OAM hologram is discussed in Supplementary Note 3.

According to diffraction theory, the dispersive response of the metasurface causes different sizes of reconstructed holographic images depending on the designed wavelength. To reconstruct holographic images with the same size for different wavelengths, the size of the original images is adjusted. The dimensions of the target objects for 450 nm and 635 nm wavelengths were adjusted to ratios of 0.84 and 1.128, respectively. Therefore, the metasurface can simultaneously reconstruct holographic images of the same size for distinct wavelengths without optical scaling (Supplementary Note 4). Consequently, a meta-hologram with a size of 255 μm by 255 μm, an effective period of 425 nm, and an effective numerical aperture of 0.05 is fabricated through a series of patterning steps that include electron-beam lithography and dry etching (Fig. 4d and e; see Methods).

Characterization of wavelength-multiplexed OAM holographic metasurface

Here, we characterize our wavelength-multiplexed OAM holographic device (Figure S5 and method). The laser beams are focused by achromatic doublet ($f_{CL1} = 3.0$ cm), then coupled to the with single mode fiber (SMF). The clean gaussian beam emitted from fiber facet is collimated by achromatic doublet ($f_{CL2} = 3.0$ cm), and become linearly polarized using linear polarizer (LP) in a proper angle to maximize efficiency of spatial light modulator (SLM). Gaussian beams spatially filtered with the fiber are illuminated onto SLM, thus generating optical vortex at each wavelength. Then, the SLM first order is circularly polarized using quarter-wave plate (QWP). The beam is finally modulated by weak focusing lens (L1) before illuminating the holographic device. The holograms are imaged after passing through QWP and LP to filter the co-polarization component. Then the captured holograms are filtered with corresponding imaging array afterwards.

Using the multiplexing method introduced in the last section, we encoded six alphabetical images into our wavelength-OAM multiplexed metasurface. Specifically, the letters 'A', 'B', and 'C' are encoded using the meta-atom MA2, thus being selectively reconstructed by a 635 nm laser. Similarly, 'G', 'H', and 'I' are reconstructed by a 473 nm laser. In terms of OAM selectivity, the letters 'A' and 'G' are selected for topological charge + 2. Similarly, 'B' and 'H' correspond to charge 0, and 'C' and 'I' correspond to charge − 2. From the measurements, the corresponding alphabet images are well reconstructed at the specific topological charge and target wavelength (Fig. 5a and b). This is illustrated by the diagonal peaks of intensity in the 3D bar charts, which correspond to the correct image and OAM mode combinations (Fig. 5c and d). There is minimal crosstalk in image 'C' when illuminated with the mode 2, but it is less than 2%, which can be considered tolerable. The second set of images, 'G', 'H', and 'I', also demonstrates clear reconstruction under their respective OAM modes, with near-zero crosstalk from other modes.

The slightly noisy images are attributed to imperfect filtering of the QWP and LP in the imaging step and fabrication errors in the lithography and etching steps. Additionally, interleaving structures in the unit pixel might lead to slight wavefront distortion at non-target wavelengths. As the OAM beam and spiral phase profile have central symmetric characteristic, alignment between incident beam and metasurface is also a factor

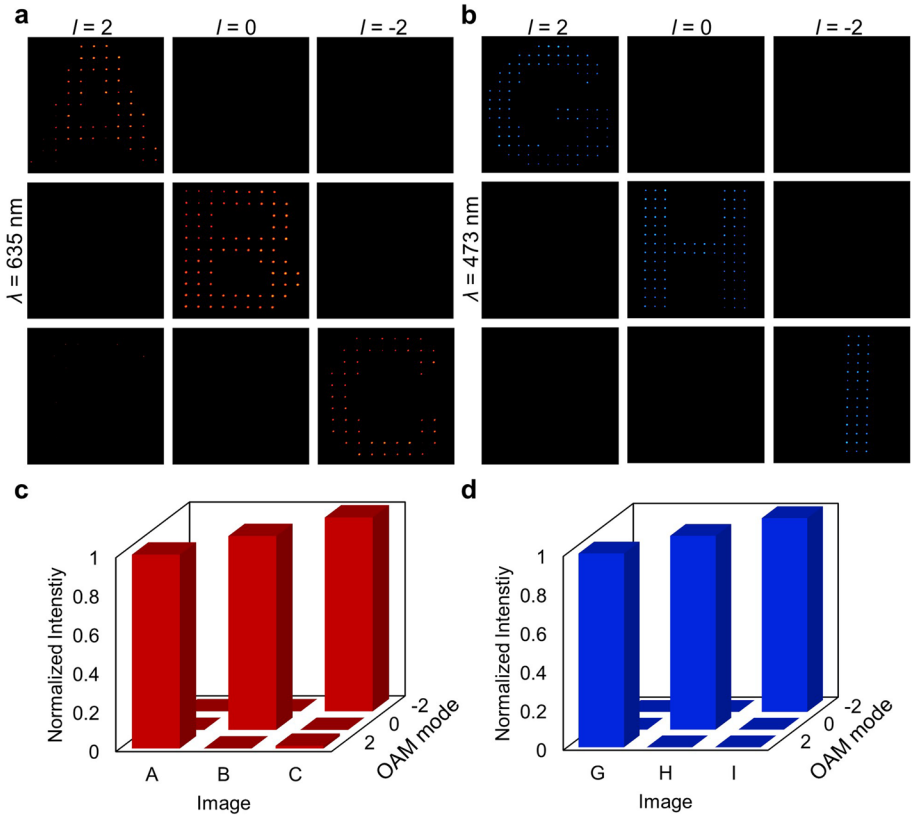

Fig. 5 Optical characterization of wavelength-multiplexed OAM holographic device. Hologram reconstruction under (**a**) 635 nm and (**b**) 473 nm with series of OAM beam. The measured intensities of the reconstructed holograms under different OAM modes with the wavelength of (**c**) 635 nm and (**d**) 473 nm. This suggests the strong OAM selectivity of wavelength-multiplexed OAM holograms

that affects holographic performance. Misalignment between the incident OAM beam and the metahologram can cause distortion and break the uniformity of the intensity distribution of the reconstructed image (Figure S6). Nevertheless, the quality of each hologram is clear, which demonstrates that our method to multiplex holograms in the wavelength and OAM domains is successful.

The crosstalk in hologram reconstruction at different wavelengths was further investigated (Supplementary Note 7). The results show a clear contrast between the 'A', 'B', and 'C' images and the 'G', 'H', and 'I' images under 635 nm illumination. However, some wavelength crosstalk is observed during reconstruction with 470 nm light, due to the fact that the conversion efficiency of MA2 (Fig. 2) is not high enough to completely suppress this crosstalk, making 'A', 'B', and 'C' slightly visible. This crosstalk, which is more noticeable than expected, may also result from fabrication imperfections. Additionally, the characterization with the 470 nm laser is less efficient since MA1 is designed to have maximum peaks at 450 nm.

Conclusion

We proposed wavelength-OAM multiplexed holography and investigated the design principles and modified algorithms to improve the quality of reconstructed holograms. This high-capacitance holography is realized using a state-of-the-art optical element, metasurface. The meta-atom, a constituent element of the metasurface, is designed to possess wavelength selectivity by engineering the dispersion of two dominant waveguide modes to achieve a phase difference close to π. The required phase at each pixel for the hologram is realized by orienting the meta-atom at the corresponding angle. As a demonstration, OAM multiplexed holography at two wavelengths was designed and fabricated by spatially interleaving two meta-atoms with target wavelengths of 450 nm and 635 nm: MA1 and MA2. In this sampling step, the sampling grid is rotated by 45° to create an effective period smaller than the minimum wavelength in this system, thus suppressing high-order diffraction and enabling large FOV hologram reconstruction. The fabricated metasurface was then characterized using a holography setup that can modulate the OAM mode index and wavelength of the incident light. Thus, we proved the wavelength and OAM selectivity of the proposed wavelength-OAM multiplexed holography.

The measured hologram efficiency at 470 nm and 635 nm are 1.38% and 12.35%, respectively. Simulated results for the grating deflection efficiency of MA1 and MA2 array 8.09% at 448 nm and 50.65% at 635 nm (Figure S9 and Table S1). Notably, recent studies on metasurface multiplexing holography report total efficiencies between 4% and 10% [5, 22], indicating that our results are reasonable with the current state of research. Fabrication errors can significantly reduce polarization conversion efficiency and cause local phase distortions, which may disrupt accurate hologram reconstruction. Additionally, optical component losses may contribute to the decrease in efficiency, although this effect is minor compared to the factors mentioned above. To address the low efficiency in the blue regime, one potential solution is to develop materials with a reasonably high refractive index and low loss [31]. Y. Yang et al. reported that hydrogenated amorphous silicon (a-Si: H) can be engineered by controlling hydrogenation and silicon disorder, which could be a promising approach to

developing such materials. Another option is to use materials with a moderate refractive index and zero loss, such as TiO_2 [30, 34] or SiN, offering a refractive index in the range of 2 to 2.6. However, with this moderate refractive index, it could be difficult to design wavelength-selective metaatoms because the nanostructures made from these materials may lack the light confinement needed to generate wavelength-specific modes.

This wavelength-OAM multiplexed holography is not limited to just two colors. Full-color holography can be realized by choosing multiple wavelengths in the design step. One factor that limits the degree of freedom is the full-width-half-maximum (FWHM) of the conversion efficiency of the meta-atom. Given that the FWHM of MA1 and MA2 are approximately 100 and 120 nm, respectively (Fig. 2), we estimate that the maximum number of spectral channels could be 3. To support this finding, we further investigated a meta-atom (MA3: l = 160 nm; w = 90 nm) with a maximum conversion efficiency around 523 nm and near zero at 450 nm and 635 nm (Supplementray Note 9 and Figure S10). This demonstrates the potential of our metasurface for future full-color applications. However, there is still some spectral overlap in the conversion efficiencies, leading to inevitable crosstalk [34]. To avoid such crosstalk, meta-atoms with narrow and defined wavelength selectivity are required. This need can be fulfilled by the concept of a nonlocal metasurface that has high-Q resonance arising from array response but can possess local phase encoding capability through local perturbation [35–37]. However, the target wavelength regime has mostly been in the NIR, not in the visible range. This is because such high-Q resonance requires materials with a high refractive index but low extinction, which silicon provides perfectly in the NIR regime. From a fabrication perspective, the feature size required for local perturbation in the visible, especially the blue regime, might be too small to fabricate using conventional techniques. Therefore, one should wisely design nonlocal metasurfaces with transparent materials with a moderate refractive index, such as TiO_2 [30, 38, 39], HfO_2 [40], and ZrO_2 [41, 42], and feasible-to-fabricate local perturbations with certain symmetry breaking. This will enable full-color OAM holography with near-zero crosstalk, potentially expanding to the realization of full-color 3D OAM holography and full-color 3D holographic video.

This wavelength-OAM multiplexed holography offers potential for expanding the number of OAM channels (Supplementary Note 9). With a 50×50 image sampling array, our metasurface can support up to 21 OAM channels, not accounting for potential crosstalk effects when using phase-only encoding for multiplexing the holograms. By fabricating a larger metasurface, the number of OAM channels can be multiplied, significantly increasing the bandwidth of our holography (Figure S11). However, As the number of OAM mode channels increases, sampling distance in the image should increase, which decrease the resolution of the image. Moreover, interference between reconstructed images of desired OAM mode and undesired OAM mode can occurs due to coherence of incident OAM beams, which cause noise and fluctuation of intensity distribution (See Figure S12). Therefore, long sampling distance and coherence of light limit the capacitance holography. Temporal multiplexing design with pseudo incoherent is one way to overcome challenges. This method is effective to suppress the interference impact on the images as well as reduce the sampling distance, which increase holography capacitance with good quality images [16].

Methods

Full-wave simulation

The in-house developed rigorous coupled wave analysis (RCWA) is used for calculating the conversion efficiency spectra and effective refractive indices of nanostructures. The electric field distribution is numerically calculated using the finite-element method (FEM). Scalar diffraction theory with the Fresnel approximation is used to predict the propagation of the vortex beam coupled to the metasurface.

Metasurface fabrication

Metasurfaces were fabricated on a 500 μm-thick glass substrate. A 900 nm-thick layer of a-Si: H was deposited using plasma enhanced chemical vapor deposition (PECVD, BMR Technology HiDep-SC) with a flow rate of 10 sccm for SiH_4 and 75 sccm for H_2. Chamber pressure and operating temperature were 30 mTorr and 100 °C, respectively. To transfer meta-atoms onto a single layer of positive tone photoresists (495 PMMA A2, MicroCehm), the standard EBL process (ELONIX, ELS-7800) was used to expose photoresist. Acceleration voltage and beam current is 80 kV and 100 pA, respectively. The exposed patterns were developed by MIBK/IPA 1:3 developer mixed solution. A 50 nm-thick chromium (Cr) layer was deposited using electron beam evaporation (KVT, KVE-ENS4004). The lift-off Cr meta-atoms were used as an etching mask for the a-Si: H film. Cr patterns were transferred onto the glass substrate using a dry etching process (DMS, silicon/metal hybrid etcher). The remaining Cr etching mask was removed by Cr etchant (CR-7).

Optical measurement

Light sources are diode lasers at the central wavelength of 635 nm (CPS635, Thorlabs) and 473 nm (PGL-VI-1-473-30mW, CNI). Input beams are filtered as clean gaussian beam through SMF (S405-XP, Thorlabs). The clean gaussian beams are modulated with spatial light modulator (SLM) (X152113-01, Hamamatsu), which yield spiral wavefronts. The beams are focused by achromatic lens (TTL 180-A, Thorlabs), then incident on metasurface. The holograms are imaged through imaging system that consists of 20x objective (LMPLFLN 20X with NA of 0.4, Olympus), tube lens (AC508-075-A-ML, Thorlabs), and camera (INFINITY 1–2, Lumenera).

Supplementary Information

The online version contains supplementary material available at https://doi.org/10.1186/s43074-024-00142-7.

Supplementary Material 1.

Acknowledgements
The authors acknowledge Seokwoo Kim for modifying the in-house RCWA code to find mode refractive index.

Authors' contributions
J.R., J.J., S.A.M. and H.R. conceived the idea and initiated the project. J.J. designed and analyzed the meta-atoms. J.K. fabricated the metasurface devices. J.J., S.-W.M. and H.R. calculated the multiplexed phase maps and conducted the propagation simulations. S.-W.M. developed the two-step algorithms. J.M. developed the in-house RCWA code. J.J. and S.-W.M. built the optical setup and conducted the holographic reconstruction measurements. All authors participated in writing the manuscript and approved the final version. J.R. guided the entire work.

Funding
This work was financially supported by the Samsung Research Funding & Incubation Center for Future Technology grant (SRFC-IT1901-52) funded by Samsung Electronics. J.R. acknowledges the POSCO-POSTECH-RIST Convergence Research

Center program funded by POSCO, and the National Research Foundation (NRF) grant (RS-2024-00356928) funded by the Ministry of Science and ICT (MSIT) of the Korean government. J.J. and J.M. acknowledge the NRF *Sejong* Science fellowships (RS-2023-00209560, RS-2023-00252778), respectively, funded by the MSIT of the Korean government. J.J. acknowledges the Hyundai Motor Chung Mong-Koo fellowship. J.K. acknowledges the Asan Foundation Biomedical Science fellowship, and the Presidential Science fellowship funded by the MSIT of the Korean government. S.A.M. acknowledges the funding support from the Lee-Lucas Chair in Physics, and the Australia Research Council (DP220102152). H.R. acknowledges the funding support from the Australian Research Council (DE220101085 and DP220102152).

Availability of data and materials
The datasets generated and/or analyzed during the current study are available from the corresponding author on reasonable request. Additionally, any code used for data analysis is available from the corresponding author upon request.

Declarations

Ethics approval and consent to participate
Not applicable.

Competing interests
The authors declare no conflict of interest.

Received: 26 June 2024 Revised: 31 August 2024 Accepted: 9 September 2024
Published online: 30 September 2024

References

1. Jang J, Badloe T, Rho J. Unlocking the future of optical security with metasurfaces. Light Sci Appl. 2021;10:144.
2. Kim I, et al. Pixelated bifunctional metasurface-driven dynamic vectorial holographic color prints for photonic security platform. Nat Commun. 2021;12:3614.
3. Kim J, et al. Photonic encryption platform via Dual-Band Vectorial metaholograms in the Ultraviolet and visible. ACS Nano. 2022;16:3546–53.
4. Kang H, et al. Tailoring high-refractive-index nanocomposites for manufacturing of ultraviolet metasurfaces. Microsyst Nanoeng. 2024;10:53.
5. Bao Y, Wen L, Chen Q, Qiu C-W, Li B. Toward the capacity Limit of 2D Planar Jones matrix with a single-layer metasurface. Sci Adv. 2021;7: eabh0365.
6. Liu S, Liu X, Yuan J, Bao J. Multidimensional information encryption and storage: when the input is light. Research. 2021;2021:7897849.
7. Kim J, et al. Dynamic hyperspectral holography enabled by inverse-designed metasurfaces with Oblique Helicoidal Cholesterics. Adv Mater. 2024;36:2311785.
8. Gopakumar M, et al. Full-colour 3D holographic augmented-reality displays with metasurface waveguides. Nature. 2024;629:791–7.
9. An J, et al. Slim-panel holographic video display. Nat Commun. 2020;11:5568.
10. Kim J, et al. Scalable Manufacturing of High-Index Atomic layer–polymer hybrid metasurfaces for Metaphotonics in the visible. Nat Mater. 2023;22:474–81.
11. Ko J, et al. Metasurface-embedded contact lenses for Holographic Light Projection. Adv Sci. 2024;11:2407045.
12. Yu P, et al. Generation of switchable singular beams with dynamic metasurfaces. ACS Nano. 2019;13:7100–6.
13. Jin L, et al. Dielectric multi-momentum meta-transformer in the visible. Nat Commun. 2019;10:4789.
14. Zhou H, et al. Polarization-encrypted orbital angular momentum multiplexed metasurface holography. ACS Nano. 2020;14:5553–9.
15. Fang X, Ren H, Gu M. Orbital angular momentum holography for high-security encryption. Nat Photon. 2020;14:102–8.
16. Shi Z, Wan Z, Zhan Z, Liu K, Liu Q, Fu X. Super-resolution orbital angular momentum holography. Nat Commun. 2023;14:1869.
17. Fang X, et al. High-dimensional orbital angular momentum multiplexing nonlinear holography. Adv Photonics. 2021;3:015001.
18. Yang H, et al. Angular Momentum Holography via a minimalist metasurface for optical nested encryption. Light Sci Appl. 2023;12:79.
19. Zhang F, Kong L-J, Zhang Z, Zhang J, Zhang X. Laguerre Gaussian Mode Holography and its application in optical encryption. Opt Express. 2023;31:12922.
20. Guo J, et al. Spatially structured-mode multiplexing holography for high-capacity security encryption. ACS Photonics. 2023;10:757–63.
21. Zhang N, Xiong B, Zhang X, Yuan X. Multiparameter encrypted orbital angular momentum multiplexed holography based on multiramp helicoconical beams. Adv Photonics Nexus. 2023;2:036013.
22. He G, et al. Multiplexed manipulation of orbital angular momentum and wavelength in metasurfaces based on arbitrary complex-amplitude control. Light Sci Appl. 2024;13:98.
23. So S, Mun J, Park J, Rho J. Revisiting the design strategies for Metasurfaces: fundamental physics, optimization, and Beyond. Adv Mater. 2023;35: 2206399.
24. Choi E, Kim G, Yun J, Jeon Y, Rho J, Baek S-H. 360° structured light with learned metasurfaces. Nat Photon. 2024;18:848–55.

25. Yoon J, Jung C, Kim J, Rho J, Lee H. Chemically and geometrically programmable photoreactive polymers for transformational humidity-sensitive full-color devices. Nat Commun. 2024;15:6470.
26. Jung C, et al. Metasurface-driven optically variable devices. Chem Rev. 2021;121:13013–50.
27. Jung C, Lee E, Rho J. The rise of electrically tunable metasurfaces. Sci Adv. 2024;10:eado8964.
28. Kang H, Kim H, Kim K, Rho J. Printable spin-multiplexed metasurfaces for Ultraviolet Holographic displays. ACS Nano. 2024;18:21504–11.
29. Ren H, et al. Publisher correction: an achromatic metafiber for focusing and imaging across the entire telecommunication range. Nat Commun. 2022;13:4321.
30. Chen WT, Park J-S, Marchioni J, Millay S, Yousef KMA, Capasso F. Dispersion-Engineered metasurfaces reaching Broadband 90% relative diffraction efficiency. Nat Commun. 2023;14:2544.
31. Yang Y, et al. Revealing Structural disorder in hydrogenated amorphous silicon for a low-loss photonic platform at visible frequencies. Adv Mater. 2021;33:2005893.
32. Ren H, Fang X, Jang J, Bürger J, Rho J, Maier SA. Complex-amplitude metasurface-based orbital angular momentum holography in momentum space. Nat Nanotechnol. 2020;15:948–55.
33. Ren H, et al. Metasurface orbital angular momentum holography. Nat Commun. 2019;10:2986.
34. So S, et al. Multicolor and 3D Holography generated by inverse-designed single-cell metasurfaces. Adv Mater. 2023;35:2208520.
35. Overvig AC, Malek SC, Yu N. Multifunctional nonlocal metasurfaces. Phys Rev Lett. 2020;125: 17402.
36. Kim M, Lee D, Kim J, Rho J. Nonlocal metasurfaces-enabled Analog Light localization for imaging and lithography. Laser Photonics Rev. 2024;18:2300718.
37. Malek SC, Overvig AC, Alù A, Yu N. Multifunctional resonant wavefront-shaping meta-optics based on multilayer and multi-perturbation nonlocal metasurfaces. Light Sci Appl. 2022;11:246.
38. Kim J, et al. A water-soluble label for food products prevents packaging waste and counterfeiting. Nat Food. 2024;5:293–300.
39. Kim J, et al. Metasurface Holography reaching the highest efficiency limit in the visible via one-step nanoparticle-embedded-Resin Printing. Laser Photonics Rev. 2022;16:2200098.
40. Zhang C, et al. Low-loss metasurface optics down to the deep ultraviolet region. Light Sci Appl. 2020;9:55.
41. Kim J, et al. One-step printable platform for high-efficiency metasurfaces down to the Deep-Ultraviolet Region. Light Sci Appl. 2023;12:68.
42. Kim J, et al. 8″ Wafer-Scale, Centimeter-Sized, high-efficiency metalenses in the Ultraviolet. Mater Today. 2024;73:9–15.

Publisher's note